PHYSICAL REVIEW D **93,** 043001 (2016)

Detailed parametrization of neutrino and gamma-ray energy spectra from high energy proton-proton interactions

A. D. Supanitsky*

Instituto de Astronomía y Física del Espacio (IAFE, CONICET-UBA), CC 67, Sucursal 28, C1428ZAA Buenos Aires, Argentina

(Received 20 October 2015; published 1 February 2016)

Gamma rays and neutrinos are produced as a result of proton-proton interactions that occur in different astrophysical contexts. The detection of these two types of messengers is of great importance for the study of different physical phenomena, related to nonthermal processes, taking place in different astrophysical scenarios. Therefore, the knowledge of the energy spectrum of these two types of particles, as a function of the incident proton energy, is essential for the interpretation of the observational data. In this paper, parametrizations of the energy spectra of gamma rays and neutrinos, originated in proton-proton collisions, are presented. The energy range of the incident protons considered extends from 10^2 to 10^8 GeV. The parametrizations are based on Monte Carlo simulations of proton-proton interactions performed with the hadronic interaction models QGSJET-II-04 and EPOS-LHC, which have recently been updated with the data taken by the Large Hadron Collider.

DOI: 10.1103/PhysRevD.93.043001

I. INTRODUCTION

Gamma rays and neutrinos can be produced in different astrophysical contexts and by different mechanisms. One of the principal production processes corresponds to the interactions undergone by accelerated protons with low energy background protons, present in different astrophysical environments [1]. An example of this is the interactions of protons accelerated in a supernova remnant with protons belonging to a nearby, or even interacting, molecular cloud [2]. Another important example is the production of gamma rays and neutrinos due to the interaction of galactic cosmic rays with the gas in the interstellar medium [3,4].

In proton-proton collisions, most of the gamma rays are produced by the decay of neutral pions generated in these interactions; η mesons also contribute to the gamma-ray spectrum. The generation of neutrinos is dominated by the decay of charged pions. Negative (positive) charged pions mainly decay into a muon (antimuon) and an antimuon (muon) neutrino,

$$\pi^- \rightarrow \mu^- + \bar{\nu}_\mu,$$
$$\pi^+ \rightarrow \mu^+ + \nu_\mu.$$

The subsequent decay of the muons and antimuons produces more neutrinos,

$$\mu^- \rightarrow e^- + \bar{\nu}_e + \nu_\mu,$$
$$\mu^+ \rightarrow e^+ + \nu_e + \bar{\nu}_\mu.$$

Many gamma-ray sources have been discovered in past years due to the ground based and also orbital gamma-ray observatories in operation at present. In fact, the third Fermi-LAT catalog has 3033 gamma-ray sources [5]. On the order hand, high energy neutrinos of astrophysical origin have recently been discovered by IceCube [6]. If the gamma rays and neutrinos are produced in proton-proton interactions in a given astrophysical object their fluxes must be strongly correlated [3,4]. Therefore, the knowledge of the energy spectra of gamma rays and neutrinos produced in proton-proton interactions is very important for the interpretation of the gamma-ray and neutrino observations.

The hadronic interactions at the highest energies are not known. However, there are models that extrapolate low energy accelerator data to the highest energies. The models Sibyll [7], QGSJET [8], EPOS [9], and PYTHIA [10] are the most commonly used in the literature. It is worth mentioning that QGSJET and EPOS have recently been updated by using the data taken by the Large Hadron Collider (LHC). The updated versions of these two models are called QGSJET-II-04 [11] and EPOS-LHC [12].

The gamma-ray energy spectrum as a function of the energy of the projectile proton has been studied extensively (see Ref. [13] and references therein). It is obtained from experimental data, at low proton energies, and from Monte Carlo simulations, at high proton energies. These Monte Carlo simulations are based on the hadronic interaction models mentioned before. In general, the gamma-ray energy spectrum is given as analytical parametrizations [13–16] or in the form of lookup tables to be interpolated [17,18].

The neutrino energy spectrum originated in proton-proton collisions has been less studied. In part, because it can be obtained, in an approximate way, from the gamma-ray energy spectrum. It is worth mentioning that this approximation is good far from the end of the neutrino energy spectrum (originated by the existence of a cutoff in

*supanitsky@iafe.uba.ar

the energy spectrum of the incident protons), but, at the end region, the difference between the approximate and the exact calculations can be quite large [19]. A widely used parametrization of the neutrino energy spectrum, valid for proton energies in the energy range from 10^2 to 10^8 GeV, is given in Ref. [14]. It is based on Monte Carlo simulations of the proton-proton interactions done by using the high energy hadronic interaction model Sibyll 2.1 [7].

In this paper, we develop parametrizations of gamma-ray and neutrino energy spectra, originated in proton-proton collisions, valid for the incident proton energy range from 10^2 to 10^8 GeV. These parametrizations are based on the hadronic interaction models QGSJET-II-04 and EPOS-LHC.

II. ENERGY SPECTRA OF GAMMA RAYS AND NEUTRINOS

A. High energy hadronic interaction models

The hadronic processes can be classified as being either soft or hard. The hard processes involve parton-parton interactions with large momentum transfer, which results into hadron jets. The soft processes correspond to interactions without a jet in which hadrons with low transverse momenta are produced. While hard interactions are very well described by perturbative quantum chromodynamics (pQCD), soft interactions do not. Therefore, the soft interactions are described by models which incorporate fundamental concepts of quantum field theory and scattering theory. Several successful models are based on the Gribov-Regge theory [20], which is by construction a multiple scattering theory. The elementary interactions are realized by complex objects called Pomerons, whose precise nature is not known.

There is a class of hadronic interaction models, which are developed mainly to interpret the data measured in accelerator experiments. PYTHIA [10], HERWIG [21], and SHERPA [22] belong to this class. In this type of models the emphasis is done in hard-scattering measurements. On the other hand, there is another class of hadronic interaction models, commonly used in cosmic-ray physics, that are able to reproduce the hadronic interactions realistically, in such a way that can reproduce accelerator data and also can provide reasonable extrapolations to higher energies and regions of the phase space where there is no available data. QGSJET and SIBYLL belong to this type of models. There is a third class of models, such as EPOS and PHOJET [23], which are designed to be more universal. They have some sophisticated descriptions of hard processes and also are able to describe experimental data in different energy ranges.

In this work QGSJET-II-04 and EPOS-LHC are considered. These two models are based on Gribov-Regge multiple scattering, pQCD, and string fragmentation. The main motivation for the use of them is that they are the updated versions of their predecessors, for which the update has been performed by using the LHC data at 7 TeV. Also the fact that the maximum proton energy considered in this work is 10^8 GeV makes them a very good option considering that, as mentioned before, they are able to extrapolate the hadronic interactions to higher energies in a reasonable way. It is worth mentioning that the differences between the predictions given by these two models have been reduced considerably after the update [24].

B. Neutrinos

Proton-proton interactions are simulated by using the package CRMC (Cosmic Ray Monte Carlo) [25], version 1.5.3. As mentioned before, the high energy hadronic interaction models QGSJET-II-04 and EPOS-LHC are used for the simulations. The energy of the projectile protons considered ranges from $\log(E_p/\mathrm{GeV}) = 2$ to $\log(E_p/\mathrm{GeV}) = 8$ in steps of $\Delta\log(E_p/\mathrm{GeV}) = 0.5$. The number of interactions simulated for each energy value is 2×10^6.

The energy spectrum of each neutrino type is calculated following Ref. [14]. These distributions are obtained from an integral that includes the energy spectra of charged pions. Therefore, let us consider the fractional energy spectrum of pions which is defined as [14]

$$F_\pi(x_\pi, E_p) = \langle n_\pi(E_p)\rangle P(E_\pi|E_p)E_p. \tag{1}$$

Here $\pi = \{\pi^+, \pi^-\}$, E_p is the energy of the projectile proton, $x_\pi = E_\pi/E_p$ where E_π is the pion energy, $\langle n_\pi\rangle$ is the average pion multiplicity, and $P(E_\pi|E_p)$ is the energy distribution of pions (normalized to one) for a given proton energy E_p. Note that

$$\frac{d\sigma_\pi}{dE_\pi}(E_\pi, E_p) = \frac{\sigma_{\mathrm{inel}}(E_p)}{E_p}F_\pi(x_\pi, E_p), \tag{2}$$

$$\int_0^1 dx_\pi F_\pi(x_\pi, E_p) = \langle n_\pi(E_p)\rangle, \tag{3}$$

where $\sigma_{\mathrm{inel}}(E_p)$ is the inelastic proton-proton cross section.

Figure 1 shows the fractional energy spectrum of charged pions, multiplied by x_π, as a function of the logarithm of x_π for two different values of the incident proton energy, $10^{2.5}$ GeV (top panel) and $10^{7.5}$ GeV (bottom panel). The high energy hadronic interaction model used is QGSJET-II-04. The solid lines correspond to a cubic spline interpolation of the simulated data.

Following Ref. [14] we denote $\nu_\mu^{(1)}$ ($\bar\nu_\mu^{(1)}$) to the neutrinos (antineutrinos) originated in the decay of π^+ (π^-), $\nu_\mu^{(2)}$ ($\bar\nu_\mu^{(2)}$) to the neutrinos (antineutrinos) originated in the decay of μ^- (μ^+), and ν_e^{np} ($\bar\nu_e^{np}$) and ν_μ^{np} ($\bar\nu_\mu^{np}$) to the electron neutrinos (antineutrinos) and muon neutrinos (antineutrinos), respectively, which do not come from the decay of neither pions nor muons originated in pion decays. Note that these last neutrino components originate mainly in kaon decays [4].

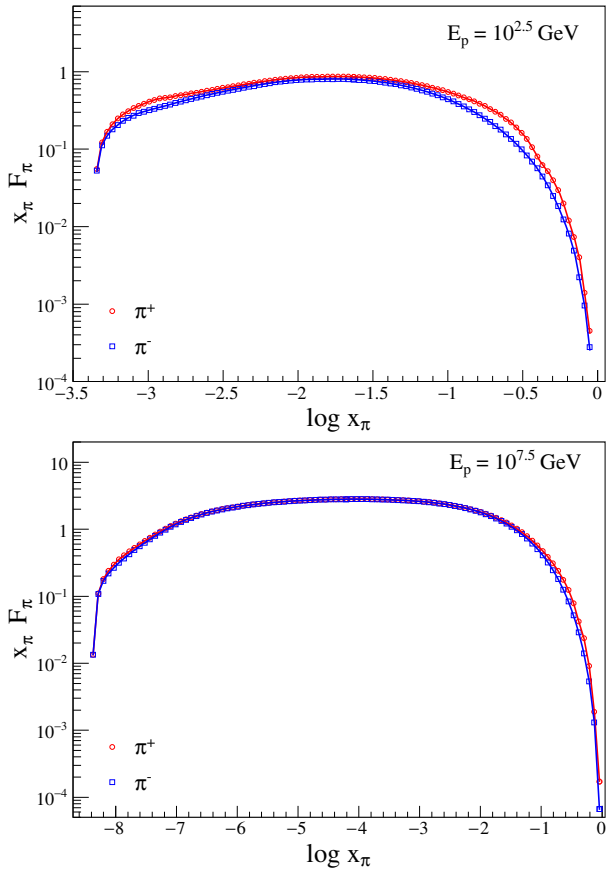

FIG. 1. Fractional energy spectra of charged pions, multiplied by x_π, as a function of $\log x_\pi$, for $E_p = 10^{2.5}$ GeV (top panel) and $E_p = 10^{7.5}$ GeV (bottom panel) and for QGSJET-II-04. Solid lines correspond to a cubic spline interpolation of the points.

The fractional energy spectrum for each type of neutrino and antineutrino, generated in charged pion decays, is given by

$$F_\nu(x_\nu, E_p) = \int_0^1 dx_\pi f_\nu\left(\frac{x_\nu}{x_\pi}\right)\frac{F_\pi(x_\pi, E_p)}{x_\pi}, \qquad (4)$$

where $\nu = \{\nu_\mu^{(1)}, \nu_\mu^{(2)}, \nu_e, \bar{\nu}_\mu^{(1)}, \bar{\nu}_\mu^{(2)}, \bar{\nu}_e\}$, $x_\nu = E_\nu/E_p$ is the neutrino energy fraction, and the functions $f_\nu(x)$ are given in Ref. [14]. Therefore, the fractional energy spectrum for this type of neutrinos and antineutrinos (the ones originated in pion decays) is calculated by using Eq. (4) and the interpolated fractional energy distributions of charged pions (see Fig. 1).

Figures 2 and 3 show the logarithm of the fractional energy spectra, as a function of the logarithm of the neutrino energy fraction, for the different types of neutrinos produced in proton-proton interactions, corresponding to $E_p = 10^{2.5}$ GeV and $E_p = 10^{7.5}$ GeV, respectively. The hadronic interaction model considered is QGSJET-II-04. The lowest value for the neutrino energy considered is 1 GeV. The bottom right panel in both figures shows, for comparison, the fitting functions corresponding to the different neutrino types displayed in the other panels. Note that the contribution of the neutrinos that do not originate in the decay of charged pions is about 1 order of magnitude smaller in almost all energy range considered. The contribution of these components becomes comparable to the one corresponding to the neutrinos originated in charged pion decays just at the end of the spectra.

The fractional energy distributions are fitted with a function of the following form:

$$F_\nu(x_\nu, E_p) = 10^{a_0(E_p) - a_1(E_p)\log(\frac{x_\nu}{x_{\rm ref}}) - a_2(E_p)\log^2(\frac{x_\nu}{x_{\rm ref}})} \times \left[\frac{1 - (\frac{x_\nu}{x_{\rm max}})^{\alpha_\nu(E_p)}}{1 - (\frac{x_{\rm ref}}{x_{\rm max}})^{\alpha_\nu(E_p)}}\right]^{\beta_\nu(E_p)} \qquad (5)$$

where a_0, a_1, a_2, α_ν, and β_ν are free fit parameters, $x_{\rm ref} = 1\ {\rm GeV}/E_p$ and $x_{\rm max} = 1$ for all types of neutrinos except for $\nu_\mu^{(1)}$ and $\bar{\nu}_\mu^{(1)}$, for which, it takes the value $x_{\rm max} = 0.427$ (see Ref. [14]). The parameters as a function of the proton energy are fitted with different types of functions in order to have a complete analytical expression of the parametrization. The parameters as a function of the proton energy for both, neutrinos and antineutrinos, are reported in Appendix A.

In Figs. 2 and 3 the ratio between the data points and the fitted function, corresponding to each neutrino type, is also shown at the bottom of each plot. It can be seen that, for each neutrino type, the difference between the fitting function and the points is, in absolute value, smaller than 20% in almost the entire energy range considered. This happens for all proton energies considered and also for the case of antineutrinos. Only at the end of the energy spectrum, after a decrease of several orders of magnitudes, the differences between the fitting function and the data points can be larger. In any case, this region is subject to larger fluctuations coming from the simulations, which makes it more difficult to obtain a better fit.

In this analysis, it is also found that the differences between neutrino and antineutrino spectra of the same type are small, as it was pointed out in Ref. [14]. For the case of neutrinos originated by the decay of charged pions, it is due to the small differences between the energy spectra of positive and negative pions. However, as it can be seen from Fig. 1, these differences are more important for smaller incident proton energies. In particular, for $E_p = 10^2$ GeV the differences between the neutrino and antineutrino energy spectra of the different cases increase with the neutrino energy, reaching values of the order of 60% in the region corresponding to the end of the spectra, except for the case of $\nu_\mu^{(2)}$, which can be as large as ~80%. For proton energies of the order of $E_p = 10^8$ GeV the differences are smaller than 20% in almost the entire energy range considered, reaching values of the order of 50% at the end of the neutrino energy spectra. In any case,

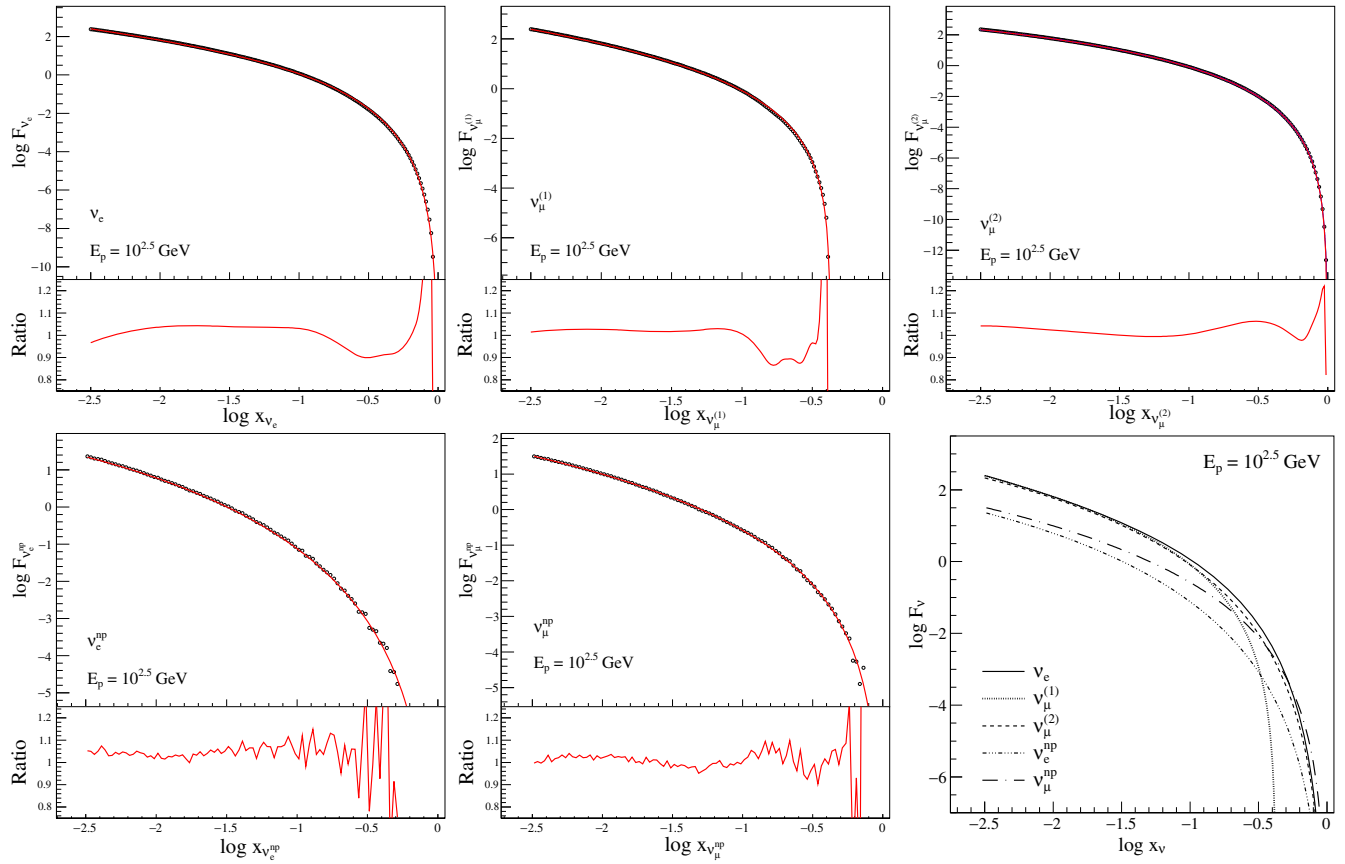

FIG. 2. Logarithm of the fractional energy distribution for each neutrino type as a function of $\log x_\nu$, for $E_p = 10^{2.5}$ GeV and for QGSJET-II-04 as the hadronic interaction model. The solid lines are fits to the distributions. The bottom right panel shows the fitting functions displayed in the other panels.

we provide fits for both neutrino and antineutrino energy spectra corresponding to each different neutrino type considered.

The fractional energy spectrum of neutrinos corresponding to EPOS-LHC is also parametrized. In this case, to fit the neutrino energy distributions is more complicated. In order to maintain the relative error of the fits smaller or of the order of 20% in almost the entire energy range, the fitting function in Eq. (5) is modified. The details of the new fitting functions and the corresponding parameters are reported in Appendix B.

C. Gamma rays

The energy spectrum of gamma rays originated in proton-proton interactions has been extensively studied (see Ref. [13] and references therein). Recently, a detailed study has been performed in Ref. [13]. In that work, a parametrization of the gamma-ray energy spectrum, for proton energies ranging from the proton-proton kinematic threshold to 1 PeV, has been obtained by combining experimental data for low energies and Monte Carlo simulations for high energies. In the high energy region they provide parametrizations done by using Geant 4.10.0 [26], PYTHIA 8.18 [10], Sibyll 2.1 [7], and QGSJET01 [8]. Therefore, these parametrizations do not include the hadronic interaction models QGSJET-II-04 and EPOS-LHC. On the other hand, the gamma-ray energy spectrum from proton-proton interactions corresponding to the QGSJET-II-04 model was presented in Ref. [17]. In this case the spectra are obtained via an interpolation between tabulated values. Also, in Ref. [18], lookup tables for the gamma-ray energy spectrum corresponding to QGSJET-II-04, EPOS-LHC, and Sibyll 2.1 are provided. However, analytical parametrizations of these distributions for QGSJET-II-04 and EPOS-LHC are not available in the literature. For that reason, an analytical parametrization for each of these two hadronic interaction models is developed in this work. The proton energy range is the one mentioned above, it starts from 10^2 GeV and extends up to 10^8 GeV. The minimum gamma-ray energy considered is 10^{-2} GeV.

A modified version of the function used in Ref. [13] is used to fit the fractional energy spectrum, which is given by

$$F_\gamma(x_\gamma, E_p) = 10^{g_0(E_p)+g_1(E_p)\log(x_\gamma)+g_2(E_p)\log^2(x_\gamma)} \times \frac{(1 - X_\gamma^{\alpha(E_p)})^{\beta(E_p)}}{(1 + \frac{X_\gamma}{C})^{\gamma(E_p)}}. \quad (6)$$

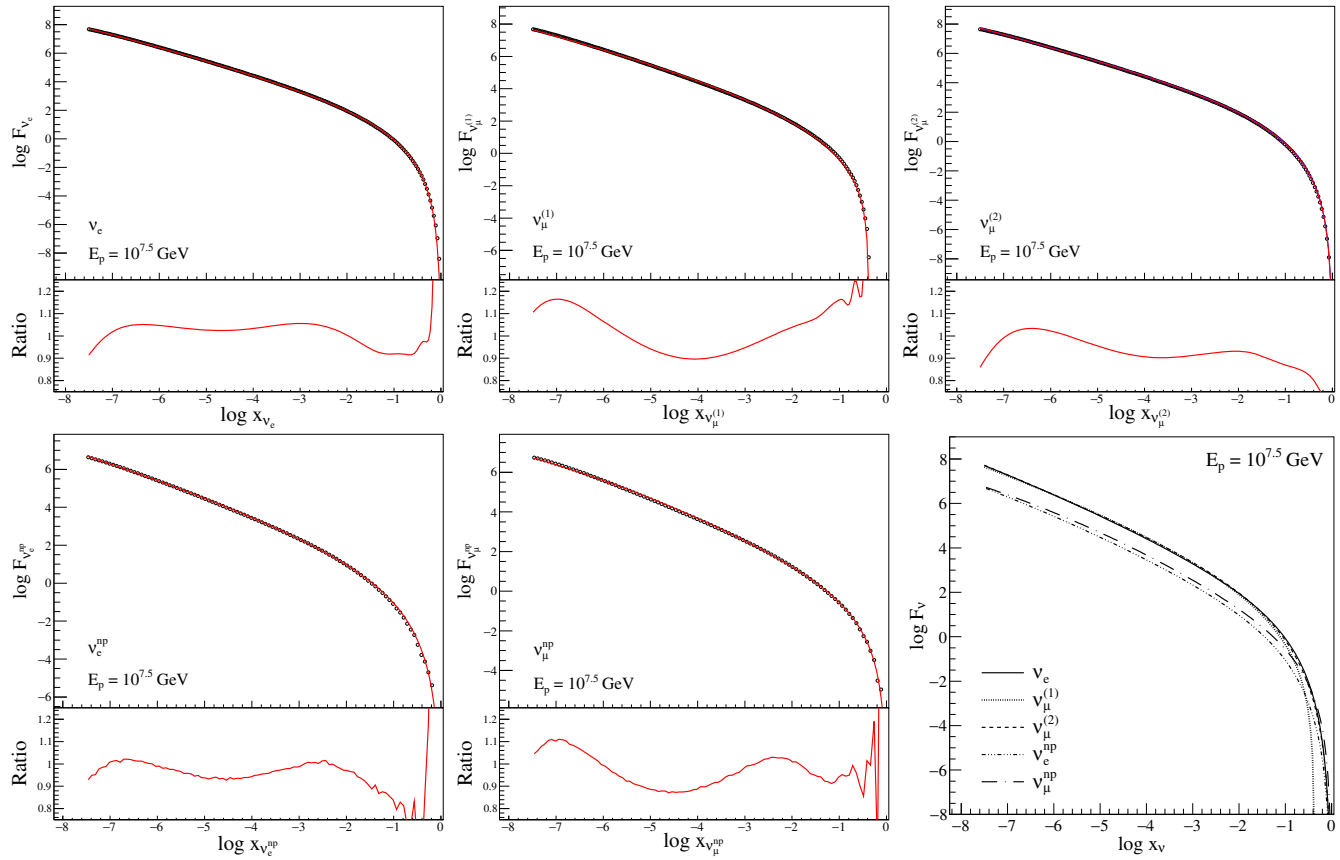

FIG. 3. Logarithm of the fractional energy distribution for each neutrino type as a function of $\log x_\nu$, for $E_p = 10^{7.5}$ GeV and for QGSJET-II-04 as the hadronic interaction model. The solid lines are fits to the distributions. The bottom right panel shows the fitting functions displayed in the other panels.

Here,

$$x_\gamma = \frac{E_\gamma}{E_p}, \tag{7}$$

$$X_\gamma = \frac{Y_\gamma - m_\pi c^2}{Y_\gamma^{\max} - m_\pi c^2}, \tag{8}$$

$$Y_\gamma = E_\gamma + \frac{m_\pi^2 c^4}{4E_\gamma}, \tag{9}$$

$$Y_\gamma^{\max} = E_\gamma^{\max} + \frac{m_\pi^2 c^4}{4E_\gamma^{\max}}, \tag{10}$$

where E_γ is the gamma-ray energy, m_π is the neutral pion mass, c is the speed of light, $E_\gamma^{\max}$ is the maximum gamma-ray energy (see Ref. [13]), and $C = \lambda m_\pi c^2 / Y_\gamma^{\max}$. Finally, g_0, g_1, g_2, α, β, γ, and λ are free fit parameters.

The parameters obtained by fitting the gamma-ray spectra corresponding to the hadronic interaction model QGSJET-II-04 are

$$\begin{aligned}
g_0(\xi) &= 2.625 + 0.3679\xi \\
g_1(\xi) &= 2.132 - 1.35285\xi + 0.2878\xi^2 - 0.02976\xi^3 \\
&\quad + 0.001175\xi^4 \\
g_2(\xi) &= 1.0429\exp(-\xi/0.8449) - 0.037 \\
\alpha(\xi) &= 0.5 \\
\beta(\xi) &= 4.5 \\
\gamma(\xi) &= 1.128\exp(-\xi/2.987) + 0.579 \\
\lambda(\xi) &= 3.55,
\end{aligned}$$

where $\xi = \log(E_p/\mathrm{GeV})$.

Figure 4 shows the fractional energy spectrum of gamma rays for three different values of the proton energy, $10^{2.5}$, 10^5, and $10^{7.5}$ GeV. The plot at the bottom in each panel corresponds to the ratio between the simulated data and the fitting function. Also in this case it can be seen that the fitting functions differ, from the data points, in less than 20% in almost the entire energy range considered. However, the differences can be larger close to the end of the spectrum. As mentioned before, this energy region is

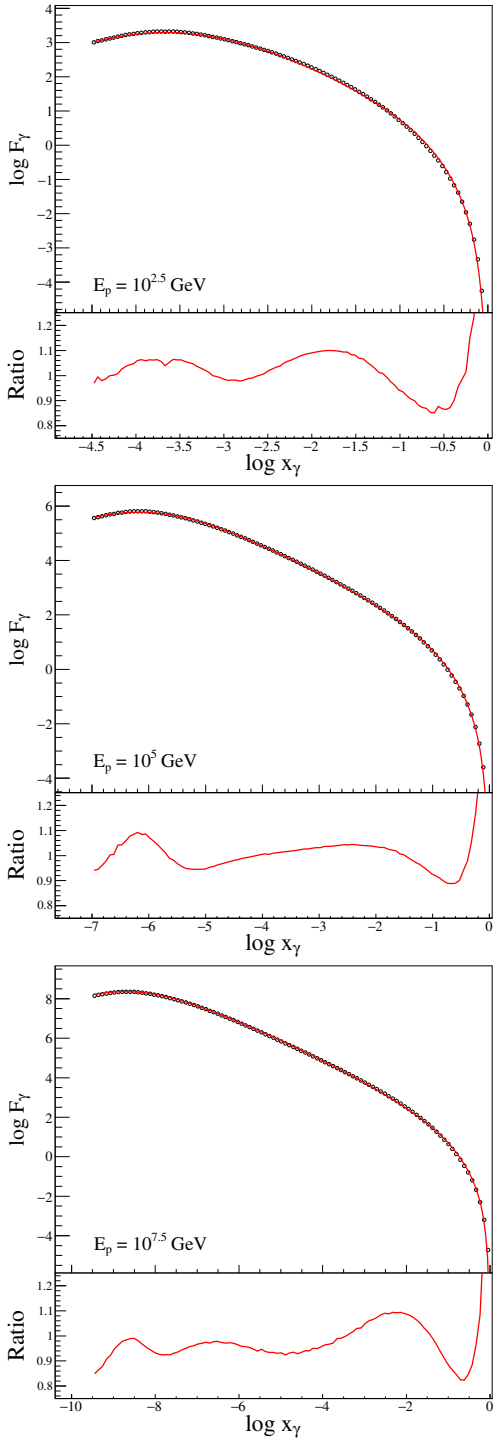

FIG. 4. Logarithm of the fractional energy distribution of the gamma rays as a function of $\log x_\gamma$, for $E_p = 10^{2.5}$, 10^5, and $10^{7.5}$ GeV and for QGSJET-II-04 as the hadronic interaction model. The solid lines are fits to the distributions.

more affected by the statistical fluctuations and then it is more difficult to fit.

The fractional energy spectrum of gamma rays corresponding to EPOS-LHC is also parametrized. The details of the parametrization and the corresponding parameters are reported in Appendix B. In this case, the same function used to fit the QGSJET-II-04 spectra is used [see Eq. (6)]. Also in this case it was more difficult to keep the relative error smaller than 20% in almost the entire energy range, which is reflected in a more complicated dependence of the fitting parameters with the incident proton energy.

D. Inelastic proton-proton cross section

The CRMC package also provides the inelastic proton-proton cross section of the hadronic model considered for the simulation. Figure 5 shows the proton-proton inelastic cross section obtained for QGSJET-II-04 and EPOS-LHC compared to the one developed by Kafexhiu *et al.* in Ref. [13].

The inelastic cross sections obtained for the two hadronic models considered are fitted with third degree polynomials in the logarithm of the projectile energy. The result of the fit corresponding to QGSJET-II-04 is given by

$$\sigma_{\text{inel}}(E_p) = [19.92 + 5.407\log(E_p/\text{GeV}) - 0.3521 \times \log^2(E_p/\text{GeV}) + 0.07887 \times \log^3(E_p/\text{GeV})]\ \text{mb}, \quad (11)$$

and the one corresponding to EPOS-LHC is given by

$$\sigma_{\text{inel}}(E_p) = [25.17 + 3.527\log(E_p/\text{GeV}) - 0.3493 \times \log^2(E_p/\text{GeV}) + 0.09784 \times \log^3(E_p/\text{GeV})]\ \text{mb}. \quad (12)$$

The fits are shown in Fig. 5. It is worth mentioning that the fits are valid in the energy range considered, i.e. from 10^2 to 10^8 GeV.

Note that, the parametrization proposed by Kafexhiu *et al.* is based on experimental data. In any case, from Fig. 5

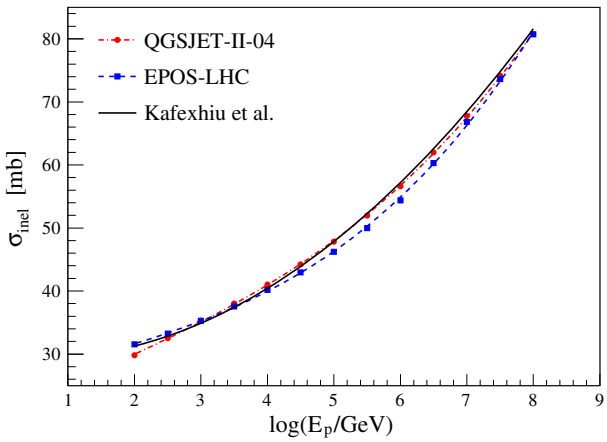

FIG. 5. Inelastic proton-proton cross section as a function of the logarithm of the projectile energy for QGSJET-II-04 and EPOS-LHC. Also shown is the fit obtained in Ref. [13]. The dashed and dash-dotted lines correspond to the fits of the simulated data with third degree polynomials (see text for details).

it can be seen that the cross sections for the two hadronic interaction models considered do not differ much from the parametrization obtained in Ref. [13]. In fact, the cross sections corresponding to these two hadronic interaction models differ in less than ∼4.5% from the one proposed by Kafexhiu *et al.*, in the energy range under consideration.

III. COMPARISON WITH OTHER PARAMETRIZATIONS

The differential cross section for gamma rays and neutrinos is given by [see Eq. (2)]

$$\frac{d\sigma_s}{dE_s}(E_s, E_p) = \frac{\sigma_{\text{inel}}(E_p)}{E_p} F_s(x_s, E_p), \tag{13}$$

where $s = \{\gamma, \nu\}$ and $x_s = E_s/E_p$.

The top panel of Fig. 6 shows the neutrino differential cross section calculated by summing the differential cross sections of the different flavors of both, neutrinos and antineutrinos. The parametrizations considered correspond to the hadronic interaction models QGSJET-II-04 and EPOS-LHC, obtained in this work, and Sibyll 2.1 obtained in Ref. [14]. The inelastic cross sections, used in Eq. (13), to calculate the differential cross section for QGSJET-II-04 and EPOS-LHC are the ones given in Eqs. (11) and (12), respectively. The inelastic cross section used for the Sibyll 2.1 parametrization is the one given in Ref. [14]. Note that the parametrizations of Ref. [14] are valid starting from $x_\nu = 10^{-3}$. The incident proton energy considered is $E_p = 10^5$ GeV. At the bottom of the top panel of Fig. 6 the ratios between the differential cross section corresponding to EPOS-LHC and Sibyll 2.1 with the one corresponding to QGSJET-II-04 are shown. It can be seen that, excluding the region corresponding to the end of the spectrum, the parametrizations corresponding to QGSJET-II-04 and EPOS-LHC differ in less than 15%. However, the parametrization provided in Ref. [14] and the ones obtained in this work differ in less than ∼35%. In both cases, the differences are much larger at the end of the spectrum. Note that a similar result is obtained in the whole energy range of the incident protons considered.

The bottom panel of Fig. 6 shows the parametrizations corresponding to the gamma-ray differential cross section for QGSJET-II-04 and EPOS-LHC, obtained in this work, and the ones corresponding to QGSJET01, Sibyll 2.1, and PYTHIA obtained in Ref. [13]. Also in this case the proton energy considered is $E_p = 10^5$ GeV and the inelastic cross sections, used in Eq. (13), to calculate the differential cross section for QGSJET-II-04 and EPOS-LHC are the ones given in Eqs. (11) and (12), respectively. At the bottom of the bottom panel of the figure, the ratios between the differential cross section corresponding to the different models considered with the one corresponding to QGSJET-II-04 are shown. It can be seen that the largest differences, in absolute value, are obtained for QGSJET01 and PYTHIA, reaching values of the order of 30%, excluding the region of the end of the spectrum, for which much larger values are obtained.

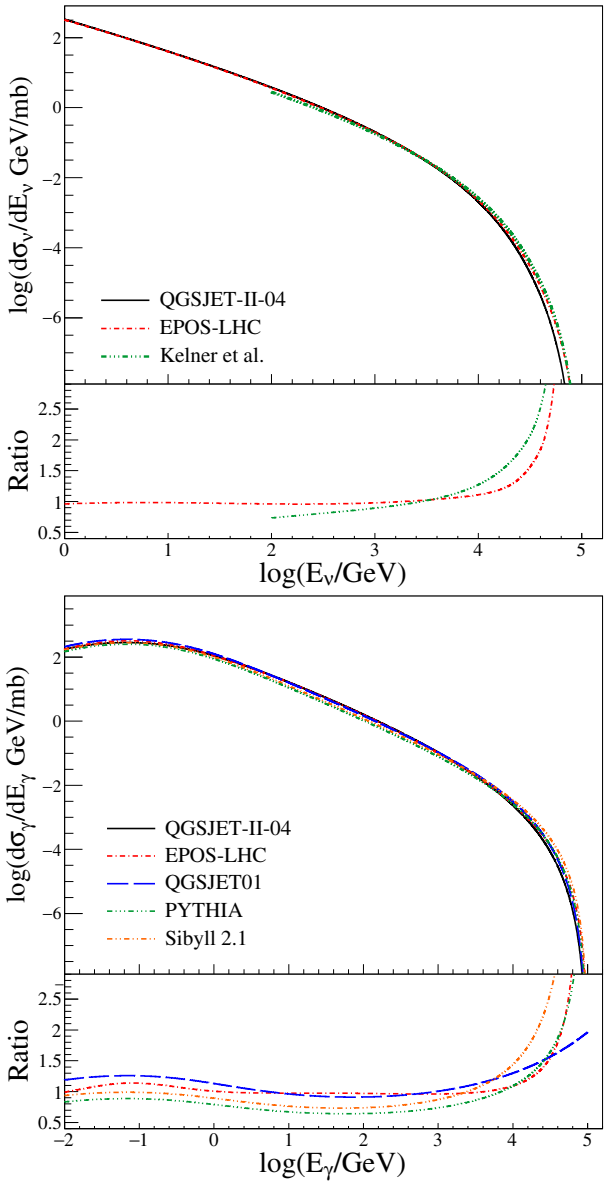

FIG. 6. Top panel: Logarithm of the neutrino differential cross section (summed over all neutrino flavors) as a function of the logarithm of the neutrino energy. Bottom panel: Logarithm of the gamma-ray differential cross section as a function of the logarithm of the gamma-ray energy. The energy of the incident protons is 10^5 GeV. At the bottom of both plots the ratios between the results obtained by using the different hadronic interaction models and the one corresponding to QGSJET-II-04 are shown.

In the case of the gamma-ray parametrizations, different behaviors are obtained as a function of the incident proton energy. Excluding the energy region corresponding to the end of the spectrum, the differences between the

parametrizations corresponding to QGSJET-II-04 and EPOS-LHC decrease with the incident proton energy, taking a maximum absolute value of the order of 20% for $E_p = 10^2$ GeV and 10% for $E_p = 10^8$ GeV. For the other models the situation is the opposite, the differences with the parametrization corresponding to QGSJET-II-04 increase with the incident proton energy, taking maximum absolute values of 20%–25% for $E_p = 10^2$ GeV and reaching to 50%–90% for $E_p = 10^8$ GeV.

In order to assess the differences due to the use of the different parametrizations in a realistic physical situation, a simple model for a nonthermal proton component present in a given astronomical object is considered. The proton energy spectrum assumed consists in a power law with an exponential cutoff,

$$\frac{dN}{dE_p} = C_0 E_p^{-\Gamma} \exp\left(-\frac{E_p}{E_{\rm cut}}\right), \tag{14}$$

where C_0 is a normalization constant, Γ is the spectral index, and $E_{\rm cut}$ is the cutoff energy. The values of the parameters adopted in this simple model are $\Gamma = 2$ and $E_{\rm cut} = 10^7$ GeV. The neutrino and gamma-ray spectra at Earth emitted by a given galactic[1] source can be written as

$$J_s(E_s) = J_0 \int_{E_s}^{\infty} dE_p \frac{d\sigma_s}{dE_s}(E_s, E_p) \frac{dN}{dE_p}(E_p), \tag{15}$$

where J_0 is a normalization constant.

Figure 7 shows the flux corresponding to the sum of the three neutrino and antineutrino flavors obtained by using QGSJET-II-04, EPOS-LHC, and Sibyll 2.1 (from Ref. [14]) parametrizations. At the bottom of the plot, the curves corresponding to the ratio between the neutrino flux, obtained by using the different parametrizations considered, and the one corresponding to QGSJET-II-04 are shown. It can be seen that the predictions corresponding to QGSJET-II-04 and EPOS-LHC are very similar for energies below the cutoff that appears in the total neutrino flux, but have larger differences in the cutoff region. The differences between the predictions corresponding to QGSJET-II-04 and Sibyll 2.1 are smaller than 20% below the cutoff but also become large in the cutoff region.

From Fig. 7 it can also be seen that the low energy part of the neutrino flux, far from the cutoff region, can be approximated by a power law. The spectral index of this power law takes values close to the spectral index of the incident proton spectrum ($\Gamma = 2$ in this case), depending on the hadronic interaction model under consideration. Considering the energy range such that $\log(E_\nu/\mathrm{GeV}) \in [2, 4]$, the spectral index takes the value ∼1.95 for QGSJET-II-04, ∼1.94 for EPOS-LHC, and ∼1.89 for Sibyll 2.1. Note that the values of the spectral index corresponding to QGSJET-II-04 and EPOS-LHC are very similar. Despite the spectral index corresponding to Sibyll 2.1 is smaller (the spectrum is harder), the difference with the ones corresponding to QGSJET-II-04 and EPOS-LHC is ∼0.05, which is quite small.

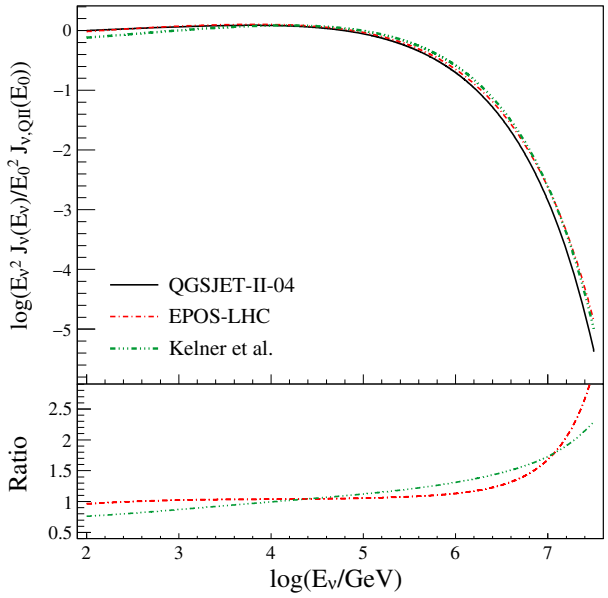

FIG. 7. Logarithm of the neutrino flux at Earth for a galactic source, multiplied by E_ν^2, as a function of the logarithm of the neutrino energy. The flux is obtained summing the contributions of every neutrino and antineutrino flavors. The parameters of the model are $\Gamma = 2$ and $E_{\rm cut} = 10^7$ GeV. The fluxes multiplied by E_ν^2 are normalized to the corresponding value obtained for QGSJET-II-04 at $E_0 = 100$ GeV. The bottom panel shows the ratios between the predictions obtained by using the different hadronic interaction models and the one corresponding to QGSJET-II-04.

Figure 8 shows the gamma-ray flux at Earth obtained for the different hadronic interaction models considered. At the bottom of the plot, the curves corresponding to the ratio between the neutrino flux, obtained by using the different parametrizations considered, and the one corresponding to QGSJET-II-04 are shown. As can be seen from the figure, the results obtained by using EPOS-LHC and PHYTIA differ in less than 10% from the one corresponding to QGSJET-II-04 for energies below the cutoff, but the differences become larger in the cutoff region. On the other hand, the results obtained by using Sibyll 2.1 and QGSJET01 differ from the one corresponding to QGSJET-II-04 in 20%–30% below the cutoff, but also in this case the differences become large in the cutoff region.

[1]Note that for an extragalactic source the energy losses, undergone by the emitted particles during propagation through the Universe, have to be taken into account in order to calculate the flux at Earth.

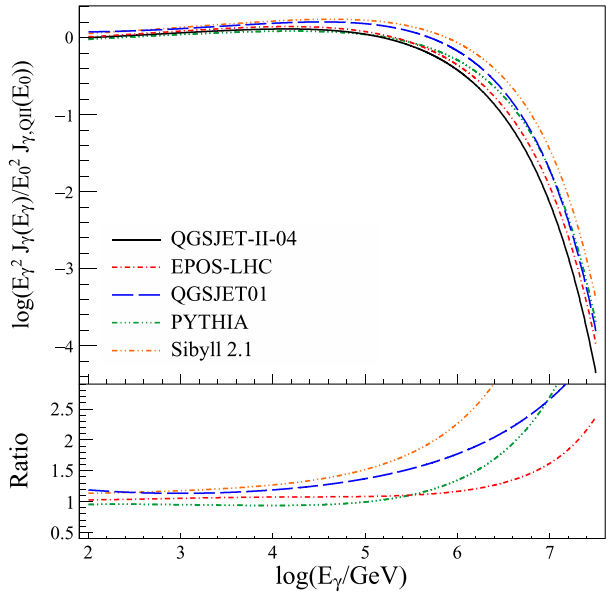

FIG. 8. Logarithm of the gamma-ray flux at Earth for a galactic source, multiplied by E_γ^2, as a function of the logarithm of the gamma-ray energy. The parameters of the model are $\Gamma = 2$ and $E_{\mathrm{cut}} = 10^7$ GeV. The fluxes multiplied by E_γ^2 are normalized to the corresponding value obtained for QGSJET-II-04 at $E_0 = 100$ GeV. The bottom panel shows the ratios between the predictions obtained by using the different hadronic interaction models and the one corresponding to QGSJET-II-04.

It is worth mentioning that the differences between the differential cross sections of both gamma rays and neutrinos obtained for QGSJET-II-04 and EPOS-LHC are small far from the end region. The same happens for the source model considered. This result is consistent with the fact that, as mentioned before, both models have been updated recently by using the data of the Large Hadron Collider.

IV. CONCLUSIONS

In this paper parametrizations of the energy spectra of gamma rays and neutrinos, generated in proton-proton interactions, are developed. The parametrizations are done for two hadronic interaction models, QGSJET-II-04 and EPOS-LHC, which have recently been updated by using the Large Hadron Collider data. The incident-proton energy considered extends from 10^2 to 10^8 GeV. The energy range for the gamma-ray spectra starts in 10^{-2} GeV and the one corresponding to neutrinos in 1 GeV. The relative error of these parametrizations is smaller than 20% in almost the entire energy range. We provide parametrizations for both neutrino and antineutrino spectra. Even though they are quite similar, they can be different in the low part of the incident proton energy interval considered in this paper.

It is worth mentioning that these types of parametrizations are of great importance to interpret the data, taken by neutrino and gamma-ray observatories, in terms of proton-proton interactions that can take place in different astrophysical scenarios.

ACKNOWLEDGMENTS

A. D. S. is a member of the Carrera del Investigador Científico of CONICET, Argentina. This work is supported by CONICET PIP 2011/360, Argentina. The author thanks to T. Pierog, C. Baus, and R. Ulrich, the authors of the CRMC package, for making it public.

APPENDIX A: PARAMETERS FOR QGSJET-II-04

The fit of the parameters is performed by using the following variable $\xi = \log(E_p/\mathrm{GeV})$, the logarithm of the incident proton energy.

The results are

(i) ν_e:

$$a_0(\xi) = -0.698 + 1.367\xi - 0.0602\xi^2 + 0.00365\xi^3$$
$$a_1(\xi) = 0.654 + 0.154\xi - 0.0276\xi^2 + 0.00149\xi^3 - 1.494 \times 10^{-5}\xi^4$$
$$a_2(\xi) = 0.00329 + 0.00324\xi$$
$$\alpha_\nu(\xi) = 0.5$$
$$\beta_\nu(\xi) = 7$$

(ii) $\bar{\nu}_e$:

$$\bar{a}_0(\xi) = -1.0368 + 1.57\xi - 0.0997\xi^2 + 0.006\xi^3$$
$$\bar{a}_1(\xi) = 0.933 - 0.0169\xi + 0.0115\xi^2 - 0.003198\xi^3 + 0.000214\xi^4$$
$$\bar{a}_2(\xi) = 0.0378$$
$$\bar{\alpha}_\nu(\xi) = 0.5$$
$$\bar{\beta}_\nu(\xi) = 7$$

(iii) $\nu_\mu^{(1)}$:

$$a_0(\xi) = -0.787 + 1.455\xi - 0.0888\xi^2 + 0.00595\xi^3$$
$$a_1(\xi) = -0.0476 + 0.281\xi - 0.048\xi^2 + 0.00419\xi^3 - 0.000133\xi^4$$
$$a_2(\xi) = 0.007$$
$$\alpha_\nu(\xi) = 0.1$$
$$\beta_\nu(\xi) = 4$$

(iv) $\bar{\nu}_\mu^{(1)}$:

$$\bar{a}_0(\xi) = -1.156 + 1.679\xi - 0.127\xi^2 + 0.00808\xi^3$$
$$\bar{a}_1(\xi) = 0.244 + 0.15\xi - 0.0168\xi^2 + 0.000292\xi^3 + 5.564\times 10^{-5}\xi^4$$
$$\bar{a}_2(\xi) = 0.007$$
$$\bar{\alpha}_\nu(\xi) = 0.1$$
$$\bar{\beta}_\nu(\xi) = 4$$

(v) $\nu_\mu^{(2)}$:

$$a_0(\xi) = -1.0855 + 1.595\xi - 0.109\xi^2 + 0.00705\xi^3$$
$$a_1(\xi) = -0.336 + 0.578\xi - 0.11\xi^2 + 0.00929\xi^3 - 0.000278\xi^4$$
$$a_2(\xi) = 2.221\exp(-\xi/0.69) + 0.00859$$
$$\alpha_\nu(\xi) = 0.3$$
$$\beta_\nu(\xi) = 6.6$$

(vi) $\bar{\nu}_\mu^{(2)}$:

$$\bar{a}_0(\xi) = -0.717 + 1.351\xi - 0.0552\xi^2 + 0.00338\xi^3$$
$$\bar{a}_1(\xi) = -0.0257 + 0.365\xi - 0.0357\xi^2 - 0.00109\xi^3 + 0.0002\xi^4$$
$$\bar{a}_2(\xi) = 0.5195 - 0.3425\xi + 0.0832\xi^2 - 0.00879\xi^3 + 0.000345\xi^4$$
$$\bar{\alpha}_\nu(\xi) = 0.4$$
$$\bar{\beta}_\nu(\xi) = 6.8$$

(vii) ν_e^{np}:

$$a_0(\xi) = -1.796 + 1.42\xi - 0.0766\xi^2 + 0.00512\xi^3$$
$$a_1(\xi) = 1.638 - 0.798\xi + 0.246\xi^2 - 0.03124\xi^3 + 0.001422\xi^4$$
$$a_2(\xi) = 0.562\exp(-\xi/1.672) + 0.0234$$
$$\alpha_\nu(\xi) = 0.45$$
$$\beta_\nu(\xi) = 6.5$$

(viii) $\bar{\nu}_e^{np}$:

$$\bar{a}_0(\xi) = -2.238 + 1.649\xi - 0.115\xi^2 + 0.0072\xi^3$$
$$\bar{a}_1(\xi) = 0.7839 - 0.3098\xi + 0.1399\xi^2 - 0.02097\xi^3 + 0.001049\xi^4$$
$$\bar{a}_2(\xi) = 1.415\exp(-\xi/1.124) + 0.0234$$
$$\bar{\alpha}_\nu(\xi) = 0.35$$
$$\bar{\beta}_\nu(\xi) = 6.5$$

(ix) ν_μ^{np}:

$$a_0(\xi) = -1.738 + 1.46\xi - 0.0744\xi^2 + 0.00408\xi^3$$
$$a_1(\xi) = 0.351 + 0.333\xi - 0.0703\xi^2 + 0.00508\xi^3 - 0.000108\xi^4$$
$$a_2(\xi) = 2.215\exp(-\xi/0.762) + 0.0511$$
$$\alpha_\nu(\xi) = 0.6$$
$$\beta_\nu(\xi) = 5$$

(x) $\bar{\nu}_\mu^{np}$:

$$\bar{a}_0(\xi) = -1.587 + 1.35\xi - 0.0622\xi^2 + 0.00416\xi^3$$
$$\bar{a}_1(\xi) = 0.995 - 0.452\xi + 0.16\xi^2 - 0.0212\xi^3 + 0.000977\xi^4$$
$$\bar{a}_2(\xi) = 0.77\exp(-\xi/1.626) + 0.0272$$
$$\bar{\alpha}_\nu(\xi) = 0.4$$
$$\bar{\beta}_\nu(\xi) = 5.$$

Note that parameters with a bar on top correspond to antineutrinos.

APPENDIX B: PARAMETRIZATION FOR EPOS-LHC

In this section the results of the fits corresponding to the hadronic interaction model EPOS-LHC are reported. In this case, two different fitting functions are considered to fit the neutrino energy spectra. These new functions are based on the one used in the case of QGSJET-II-04 [see Eq. (5)]. Note that these modifications are required to keep the relative error of the parametrizations smaller than ~20% in the major part of the neutrino energy range.

The fractional energy distributions corresponding to $\nu_\mu^{(1)}$, $\nu_\mu^{(2)}$, ν_e, $\bar{\nu}_\mu^{(1)}$, $\bar{\nu}_\mu^{(2)}$, and $\bar{\nu}_e$ are fitted with the following function:

$$\tilde{F}_\nu(x_\nu, E_p) = F_\nu(x_\nu, E_p) \times 10^{\varepsilon(E_p)\beta(E_p)[(\frac{x_\nu}{x_{\max}})^{\alpha(E_p)} - (\frac{x_{\mathrm{ref}}}{x_{\max}})^{\alpha(E_p)}]}, \quad \text{(B1)}$$

where ε is a new free parameter and $F_\nu(x_\nu, E_p)$ is given by Eq. (5).

For ν_μ^{np}, ν_e^{np}, $\bar{\nu}_\mu^{np}$, and $\bar{\nu}_e^{np}$ the fitting function considered is given by

$$\hat{F}_\nu(x_\nu, E_p) = F_\nu(x_\nu, E_p) 10^{-a_3(E_p)\log^3(\frac{x_\nu}{x_{\mathrm{ref}}})}, \quad \text{(B2)}$$

where a_3 is a new free parameter and $F_\nu(x_\nu, E_p)$ is given by Eq. (5).

Figure 9 shows the logarithm of the fractional energy spectra, as a function of the logarithm of the neutrino energy fraction, for the different types of neutrinos produced in proton-proton interactions. The incident proton energy considered is $E_p = 10^5$ GeV. The lowest value of the neutrino energy considered is 1 GeV. The bottom right panel in the figure shows, for comparison, the fitting functions corresponding to the different neutrino types displayed in the other panels. Also in this case, the ratio between the data points and the fitted function, corresponding to each neutrino type, is shown at the bottom of each plot. The difference between the fitting function and the points is smaller, in absolute value, than 20% in almost the entire energy range considered. As in the case of QGSJET-II-04, the ratio can be larger in the region corresponding to the end of the spectra.

The parameters as a function of $\xi = \log(E_p/\mathrm{GeV})$ are

(i) ν_e:

$$a_0(\xi) = -0.5316 + 1.248\xi - 0.03684\xi^2 + 0.002347\xi^3$$
$$a_1(\xi) = 5.157\xi^{-2.5} - 7.404\exp[-(\xi/1.356)^{1.595}] + 0.7979$$
$$a_2(\xi) = -0.2837\exp[-(\xi/3.061)^3)] + 0.02954$$
$$\alpha_\nu(\xi) = 0.5$$
$$\beta_\nu(\xi) = 4.5$$
$$\varepsilon(\xi) = -0.7535\exp[-(\xi/3.044)^3] - 0.2542$$

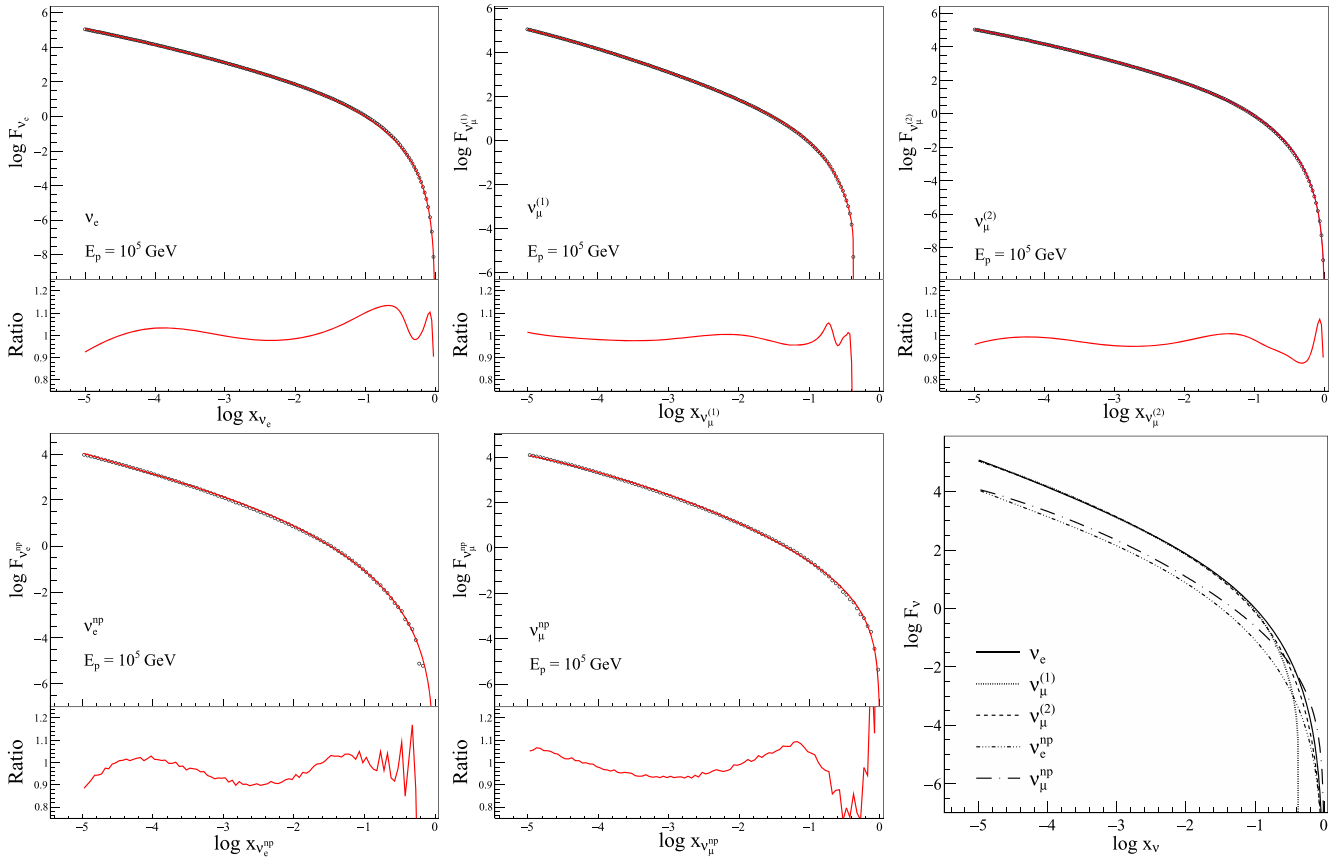

FIG. 9. Logarithm of the fractional energy distribution for each neutrino type as a function of $\log x_\nu$, for $E_p = 10^5$ GeV and for EPOS-LHC as the hadronic interaction model. The solid lines are fits to the distributions. The bottom right panel shows the fitting functions displayed in the other panels.

(ii) $\bar{\nu}_e$:

$$\bar{a}_0(\xi) = -0.7106 + 1.328\xi - 0.05061\xi^2 + 0.003194\xi^3$$
$$\bar{a}_1(\xi) = 1.828\xi^{-2} - 6.147\exp[-(\xi/1.045)^{1.207}] + 0.8$$
$$\bar{a}_2(\xi) = -0.1549\exp[-(\xi/2.92)^3] + 0.02839$$
$$\bar{\alpha}_\nu(\xi) = 0.5$$
$$\bar{\beta}_\nu(\xi) = 4.2$$
$$\bar{\varepsilon}(\xi) = -0.6735\exp[-(\xi/2.955)^3] - 0.49$$

(iii) $\nu_\mu^{(1)}$:

$$a_0(\xi) = -0.3958 + 1.156\xi - 0.02026\xi^2 + 0.001385\xi^3$$
$$a_1(\xi) = 3.392 - 1.706\xi + 0.4205\xi^2 - 0.04615\xi^3 + 0.001896\xi^4$$
$$a_2(\xi) = 0.7751\xi^{-1.165} - 1.581\exp[-(\xi/1.289)^{1.84}] - 0.03089$$
$$\alpha_\nu(\xi) = -2(\xi-2)/15 + 1.5$$
$$\beta_\nu(\xi) = 0.5865 + 0.1113\xi$$
$$\varepsilon(\xi) = -9.808 + 4.881\xi - 1.174\xi^2 + 0.1292\xi^3 - 0.005304\xi^4$$

(iv) $\bar{\nu}_\mu^{(1)}$:

$$\bar{a}_0(\xi) = -0.6812 + 1.315\xi - 0.05028\xi^2 + 0.003293\xi^3$$
$$\bar{a}_1(\xi) = 2.223 - 0.8497\xi + 0.1954\xi^2 - 0.0204\xi^3 + 0.0008075\xi^4$$
$$\bar{a}_2(\xi) = 1.881\xi^{-2.078} + 0.9213\exp[-(\xi/1.597)^{-4.198}] - 0.9061$$
$$\bar{\alpha}_\nu(\xi) = -0.05(\xi-2) + 1$$
$$\bar{\beta}_\nu(\xi) = 1.405 - 0.03499\xi$$
$$\bar{\varepsilon}(\xi) = -3.527 + 1.01\xi - 0.1967\xi^2 + 0.01045\xi^3$$

(v) $\nu_\mu^{(2)}$:

$$a_0(\xi) = -0.64897 + 1.268\xi - 0.03652\xi^2 + 0.002139\xi^3$$
$$a_1(\xi) = 0.7065\xi^{-1.5} - 10.22\exp[-(\xi/0.674)^{1.196}] + 0.7539$$
$$a_2(\xi) = -0.2364 + 0.2412\xi - 0.067356\xi^2 + 0.007829\xi^3 - 0.0003306\xi^4$$
$$\alpha_\nu(\xi) = 0.6$$
$$\beta_\nu(\xi) = 4.5$$
$$\varepsilon(\xi) = -1.688 + 0.6948\xi - 0.1184\xi^2 + 0.006386\xi^3$$

(vi) $\bar{\nu}_\mu^{(2)}$:

$$\bar{a}_0(\xi) = -0.3917 + 1.141\xi - 0.01276\xi^2 + 0.00067172\xi^3$$
$$\bar{a}_1(\xi) = 6.57\xi^{2.5} - 28.11\exp[-(\xi/0.7013)^{1.099}] + 0.7657$$
$$\bar{a}_2(\xi) = -0.4861 + 0.2386\xi - 0.03531\xi^2 + 0.001703\xi^3$$
$$\bar{\alpha}_\nu(\xi) = 0.6$$
$$\bar{\beta}_\nu(\xi) = 4.5$$
$$\bar{\varepsilon}(\xi) = -1.62 + 0.5806\xi - 0.08236\xi^2 + 0.003744\xi^3$$

(vii) ν_e^{np}:

$$a_0(\xi) = -1.852 + 1.315\xi - 0.036195\xi^2 + 0.001862\xi^3$$
$$a_1(\xi) = 0.3124 + 0.1796\xi - 0.01298\xi^2$$
$$a_2(\xi) = 3.063\xi^{-1.908} - 2.087\exp[-(\xi/1.058)^{0.3901}] + 0.14453$$
$$a_3(\xi) = \exp[-2.177 - 0.3613\xi]$$
$$\alpha_\nu(\xi) = 0.3$$
$$\beta_\nu(\xi) = 4$$

(viii) $\bar{\nu}_e^{np}$:

$$\bar{a}_0(\xi) = -2.035 + 1.287\xi - 0.01062\xi^2 - 0.0008165\xi^3$$
$$\bar{a}_1(\xi) = 0.144 + 0.2289\xi - 0.01841\xi^2$$
$$\bar{a}_2(\xi) = 3.9\xi^{-2.39} - 1.703\exp[-(\xi/0.7363)^{0.3991}] + 0.1034$$
$$\bar{a}_3(\xi) = \exp[-2.161 - 0.4299\xi]$$
$$\bar{\alpha}_\nu(\xi) = 0.3$$
$$\bar{\beta}_\nu(\xi) = 4.5$$

(ix) ν_μ^{np}:

$$a_0(\xi) = -1.571 + 1.232\xi - 0.02757\xi^2 + 0.001435\xi^3$$
$$a_1(\xi) = 0.65$$
$$a_2(\xi) = \exp[2.434 - 2.173\xi + 0.3896\xi^2 - 0.03449\xi^3 + 0.001168\xi^4]$$
$$a_3(\xi) = 0$$
$$\alpha_\nu(\xi) = 0.5$$
$$\beta_\nu(\xi) = 1.755 + 0.1818\xi$$

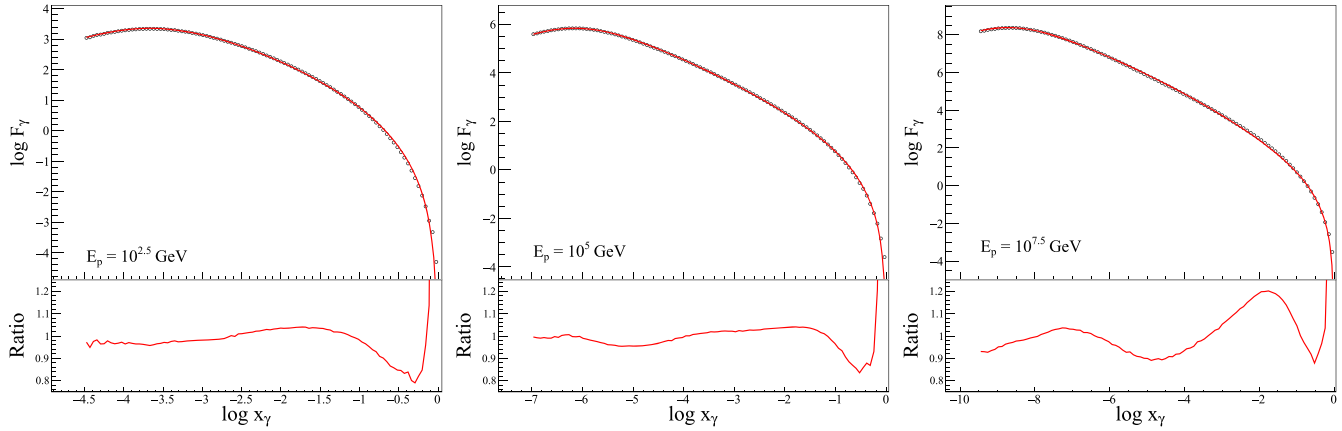

FIG. 10. Logarithm of the fractional energy distribution of the gamma rays as a function of $\log x_\gamma$, for $E_p = 10^{2.5}$, 10^5, and $10^{7.5}$ GeV and for EPOS-LHC as the hadronic interaction model. The solid lines are fits to the distributions.

(x) $\bar{\nu}_\mu^{np}$:

$$\bar{a}_0(\xi) = -1.506 + 1.184\xi - 0.02049\xi^2 + 0.001157\xi^3$$
$$\bar{a}_1(\xi) = 0.65$$
$$\bar{a}_2(\xi) = \exp[3.674 - 3.508\xi + 0.7973\xi^2 - 0.08486\xi^3 + 0.003393\xi^4]$$
$$\bar{a}_3(\xi) = 0$$
$$\bar{\alpha}_\nu(\xi) = 0.5$$
$$\bar{\beta}_\nu(\xi) = 4.1.$$

For the model EPOS-LHC, the same function used to fit the fractional energy distribution of gamma rays corresponding to QGSJET-II-04 is used [see Eq. (6)]. Figure 10 shows the fractional energy spectrum for three different values of the incident proton energy, $10^{2.5}$, 10^5, and $10^{7.5}$ GeV. The plot at the bottom in each panel corresponds to the ratio between the simulated data and the fitting function. Also in this case it can be seen that the fitting function differs in less that 20% in almost the entire energy range considered, except in the region corresponding to the end of the spectrum where the differences can be larger.

The parameters obtained by fitting the gamma-ray energy spectra corresponding to EPOS-LHC are

$$g_0(\xi) = -1.25 + 1.665\xi - 0.1234\xi^2 + 0.0008117\xi^3$$
$$g_1(\xi) = -3.489 + 2.543\xi - 0.8434\xi^2 + 0.1379\xi^3 - 0.0114417\xi^4 + 0.0003809\xi^5$$
$$g_2(\xi) = -1.963\exp(-\xi/0.6511) - 0.04743$$
$$\alpha(\xi) = 0.5$$
$$\beta(\xi) = 3.5$$
$$\gamma(\xi) = -0.001275 + 0.5269\xi - 0.1266\xi + 0.0126\xi^3 - 0.0004893\xi^4$$
$$\lambda(\xi) = 2.5,$$

where also here $\xi = \log(E_p/\mathrm{GeV})$.

It is worth mentioning that the relative error of the fits corresponding to EPOS-LHC is on average slightly larger than the corresponding one to QGSJET-II-04. In fact, as mentioned before, for EPOS-LHC extra terms have been added to the fitting function used to fit the QGSJET-II-04 neutrino spectra, in order to keep the relative error smaller than ~20% in most of the energy range considered.

[1] V. Ginzburg and S. Syrovatskii, *Origin of Cosmic Rays* (MacMillan, New York, 1964).
[2] P. Slane, A. Bykov, D. Ellison, G. Dubner, and D. Castro, Space Sci. Rev. **188**, 187 (2015).
[3] V. Berezinsky, S. Bulanov, V. Dogiel, V. Ginzburg, and S. Ptuskin, *Astrophysics of Cosmic Rays* (North-Holland, Amsterdam, 1990).
[4] T. Gaisser, *Cosmic Rays and Particle Physics* (Cambridge University Press, Cambridge, England, 1990).
[5] M. Ackermann *et al.*, Astrophys. J. **218**, 23 (2015).
[6] M. Aartsen *et al.* (IceCube Collaboration), Science **342**, 1242856 (2013).
[7] R. Fletcher, T. Gaisser, P. Lipari, and T. Stanev, Phys. Rev. D **50**, 5710 (1994).

[8] N. Kalmykov, S. Ostaphenko, and A. Pavlov, Nucl. Phys. B, Proc. Suppl. **52**, 17 (1997).
[9] K. Werner, F. M. Liu, and T. Pierog, Phys. Rev. C **74**, 044902 (2006).
[10] T. Sjöstrand, S. Mrenna, and P. Skands, Comput. Phys. Commun. **178**, 852 (2008).
[11] S. Ostapchenko, Phys. Rev. D **83**, 014018 (2011).
[12] T. Pierog, I. Karpenko, J. M. Katzy, E. Yatsenko, and K. Werner, Phys. Rev. C **92**, 034906 (2015).
[13] E. Kafexhiu, F. Aharonian, A. M. Taylor, and G. S. Vila, Phys. Rev. D **90**, 123014 (2014).
[14] S. Kelner, F. Aharonian, and V. Bugayov, Phys. Rev. D **74**, 034018 (2006); **79**, 039901(E) (2009).
[15] T. Kamae, N. Karlsson, T. Mizuno, T. Abe, and T. Koi, Astrophys. J. **647**, 692 (2006).
[16] C. Dermer, Astron. Astrophys. **157**, 223 (1986).
[17] M. Kachelrieß and S. Ostapchenko, Phys. Rev. D **86**, 043004 (2012).
[18] D. Atri and B. Hariharan, arXiv:1309.2360.
[19] A. D. Supanitsky, Phys. Rev. D **89**, 023501 (2014).
[20] V. Gribov, Sov. Phys. JETP **26**, 414 (1968).
[21] G. Corcella, I. G. Knowles, G. Marchesini, S. Moretti, K. Odagiri, P. Richardson, M. H. Seymour, and B. R. Webber, J. High Energy Phys. 01 (2001) 010.
[22] T. Gleisberg, S. Höche, F. Krauss, M. Schönherr, S. Schumann, F. Siegert, and J. Winter, J. High Energy Phys. 02 (2009) 007.
[23] R. Engel and J. Ranft, Phys. Rev. D **54**, 4244 (1996).
[24] T. Pierog, J. Phys. Conf. Ser. **409**, 012008 (2013).
[25] https://web.ikp.kit.edu/rulrich/crmc.html.
[26] S. Agostinelli *et al.*, Nucl. Instrum. Methods Phys. Res., Sect. A **506**, 250 (2003).